PNAS RESEARCH ARTICLE | APPLIED PHYSICAL SCIENCES

Transition metal dichalcogenide nanospheres for high-refractive-index nanophotonics and biomedical theranostics

Gleb I. Tselikov[a,b,1], Georgy A. Ermolaev[a,b,1], Anton A. Popov[c], Gleb V. Tikhonowski[c], Daria A. Panova[a], Alexey S. Taradin[a], Andrey A. Vyshnevyy[a,b], Alexander V. Syuy[a,b], Sergey M. Klimentov[c], Sergey M. Novikov[a], Andrey B. Evlyukhin[d], Andrei V. Kabashin[e,2], Aleksey V. Arsenin[a,b], Kostya S. Novoselov[f,g,h,2], and Valentyn S. Volkov[a,b,2]

Contributed by Kostya S. Novoselov; received May 23, 2022; accepted August 23, 2022; reviewed by Pavel Ginzburg and Maria Kafesaki

Recent developments in the area of resonant dielectric nanostructures have created attractive opportunities for concentrating and manipulating light at the nanoscale and the establishment of the new exciting field of all-dielectric nanophotonics. Transition metal dichalcogenides (TMDCs) with nanopatterned surfaces are especially promising for these tasks. Still, the fabrication of these structures requires sophisticated lithographic processes, drastically complicating application prospects. To bridge this gap and broaden the application scope of TMDC nanomaterials, we report here femtosecond laser-ablative fabrication of water-dispersed spherical TMDC (MoS_2 and WS_2) nanoparticles (NPs) of variable size (5 to 250 nm). Such NPs demonstrate exciting optical and electronic properties inherited from TMDC crystals, due to preserved crystalline structure, which offers a unique combination of pronounced excitonic response and high refractive index value, making possible a strong concentration of electromagnetic field in the NPs. Furthermore, such NPs offer additional tunability due to hybridization between the Mie and excitonic resonances. Such properties bring to life a number of nontrivial effects, including enhanced photoabsorption and photothermal conversion. As an illustration, we demonstrate that the NPs exhibit a very strong photothermal response, much exceeding that of conventional dielectric nanoresonators based on Si. Being in a mobile colloidal state and exhibiting superior optical properties compared to other dielectric resonant structures, the synthesized TMDC NPs offer opportunities for the development of next-generation nanophotonic and nanotheranostic platforms, including photothermal therapy and multimodal bioimaging.

nanooptics | 2D materials | transition metal dichalcogenides | laser ablation

Significance

Transition metal dichalcogenides offer a number of exciting physical phenomena in optics, optoelectronics, and many-body physics. At the same time, these materials offer a number of opportunities for applications. One of the biggest challenges is the mass production of high-quality nanostructures based on such materials. We propose an approach based on femtosecond laser ablation in liquids for the fabrication of water-dispersed ultrastable spherical transition metal dichalcogenide (TMDC) nanoparticles of variable size (5 to 250 nm). Such nanoparticles demonstrate very exciting optical and electronic properties inherited from the TMDC crystals, due to preserved crystalline structure, which offers a unique combination of pronounced excitonic response and high refractive index value, making possible a strong concentration of electromagnetic field in nanoparticles.

Interest in layered materials (1) has exploded in the last decade, with applications spanning from electronics (2, 3) and photonics (4, 5) to medicine (6, 7). In particular, the family of transition metal dichalcogenides (TMDCs), most notably MoS_2 and WS_2, greatly accelerated the progress in compact photodetectors (8, 9), electro- and photocatalysis (10, 11), ultrasensitive detectors (12, 13), and cancer therapies (14, 15). TMDCs exhibit a strong excitonic response, leading to nontrivial optical phenomena enabled by strong light–matter interactions: exciton–polariton transport (16, 17), enhanced second and third harmonic generation (18, 19), high refractive index, and giant optical anisotropy (17, 20, 21). Motivated by these benefits, novel TMDC nanostructures are being rapidly developed. Typically, such nanostructures are produced by electron beam lithography (22), reactive ion etching (23), focused ion beam (24), or laser thinning (25, 26). Despite their effectiveness, all of these methods have a relatively low throughput and create nanostructures formed in place and immobilized on a substrate, significantly limiting their applicability.

Pulsed laser ablation in liquids has recently emerged as a novel pathway to synthesize nanoparticles (NPs). In this technique the production of nanoclusters is done through the action of pulsed laser radiation on a solid target, followed by their release into a liquid ambient to form colloidal NP solutions (27, 28). This method is exceptionally efficient in the case of ultrashort (femtosecond) regime of laser ablation, known as a "fine" regime, which makes possible excellent control of NP size and the conservation of physicochemical properties of the bulk original material (29–31). Our previous studies illustrate a high efficiency of femtosecond laser ablation in the fabrication of a variety of nanomaterials exhibiting unique structural and optical properties, including Au (29, 30), Si (31), TiN (32), Bi (33) NPs, and Au–Si nanocomposites (34), which promises its successful use for other classes of materials. Recent publications (7, 35) tried to adopt a laser-ablative technique to obtain MoS_2 NPs. However, produced NPs

Reviewers: P.G., School of electrical engineering, Tel Aviv University; and M.K., Idryma Technologias kai Ereunas.

The authors declare no competing interest.

[1]G.I.T. and G.A.E. contributed equally to this work.

[2]To whom correspondence may be addressed. Email: andrei.kabashin@univ-amu.fr, kostya@nus.edu.sg or volkov.vs@mipt.ru.

This article contains supporting information online at http://www.pnas.org/lookup/suppl/doi:10.1073/pnas.2208830119/-/DCSupplemental.

Published September 19, 2022.

in these works are only partially crystalline, and as a result they lack excitonic response and high refractive index, which are crucial in nanophotonics. The amorphous structure reported in these works is most likely due to the nanosecond laser pulse duration, which is longer than the electron–phonon cooling time (usually several picoseconds), determining the process kinetics. Hence, achieving crystalline laser-ablated TMDC NPs for photonic applications remains a standing challenge.

Here, we explore the technique of femtosecond laser ablation in water for the synthesis of nanostructures based on TMDCs (MoS_2 and WS_2). We show that the femtosecond laser-ablative process results in the production of nearly spherical MoS_2 and WS_2 NPs, ranging from 5 nm to hundreds of nanometers. We also show that the synthesized NPs conserve crystal structure and, more crucially, high refractive index and excitonic properties of the original crystals. As a result, they exhibit distinct Mie resonances and provide a significantly improved photothermal performance compared to conventional dielectric nanoresonators in the optical transparency window of biological tissue. The proposed approach opens up the substrate-free nanofabrication of functional TMDC nanostructures, which promises tremendous potential for nanophotonic and biomedical applications.

Results and Discussion

Laser Ablation Synthesis of TMDC NPs. For the production of MoS_2 and WS_2 NPs from bulk crystal (Fig. 1*A*), we adopted the methods of ultrashort pulsed laser ablation (29–31) (*Methods*) in water, as illustrated in Fig. 1*B*. Within a few minutes of the procedure, we observed a green-brownish coloration of the solution, indicating the formation of TMDC NPs (Fig. 1*C*). Synthesized colloids were extremely stable, showing practically no signs of aggregation or precipitation even after months of storage at room temperature. This remarkable stability of colloidal solutions can be attributed to a significant charge of the NP surface identical to the process found for gold NPs (30). It should be noted that we employed a high-numerical-aperture objective to increase laser fluence and thus maximize laser ablation efficiency, but such a geometry results in a high fluence gradient and, hence, in a relatively broad size distribution (28).

We centrifuged colloidal solutions at increasing rotation speeds of 200 to 8,000 rpm to achieve monodisperse size distribution and remove the smallest (<10 nm) NPs (*Methods*). Then, size distributions of the formed colloids were assessed by the analysis of scanning electron microscopy (SEM) images of NPs (*Methods*). As expected, after the centrifugation at high rotation speed the solutions exhibited a narrow lognormal distribution presented in Fig. 1*D*. In addition, the colloids centrifuged under different conditions had smoothly changing hues (Fig. 1*C*) due to variable size and material's high dielectric permittivity (Fig. 1*E* and *SI Appendix*, Fig. S1) acquired by ellipsometry (*Methods*). Therefore, pronounced colors already indicate that NPs retain optical characteristics of the original crystal. As described in the following sections, we also performed extensive morphological and optical analyses to establish this result quantitatively.

Morphology of TMDC NPs. SEM (Fig. 2*A* and *SI Appendix*, Fig. S2*A*) shows that the produced NPs have a polygonal shape close to spherical. Conceivably, this shape results from TMDCs' edges, which tend to organize along crystallographic edges (23). The energy-dispersive X-ray spectrum in Fig. 2*A*, *Inset* confirms the predominant atomic composition of the original crystal with little oxygen present (less than 5%). Oxygen may have been

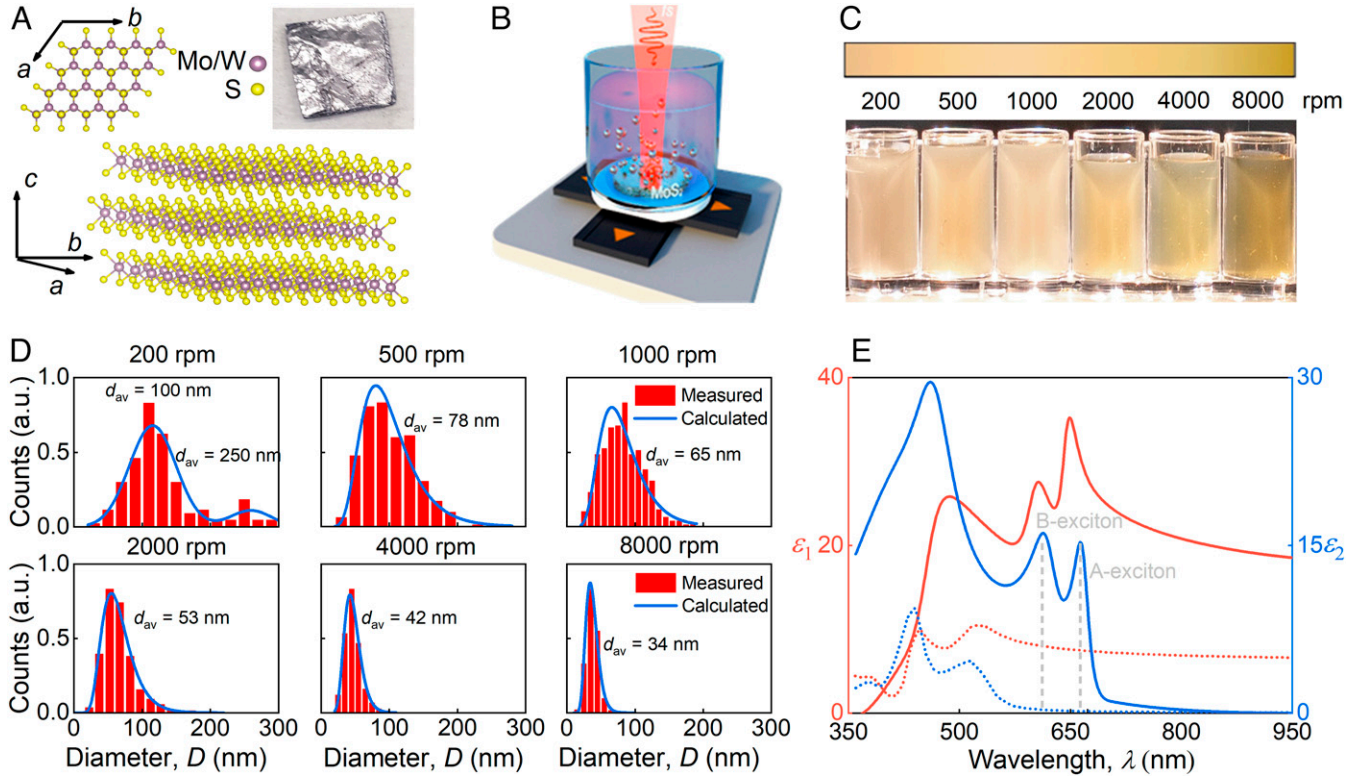

Fig. 1. Engineering of MoS_2 NPs. (*A*) Illustration of the MoS_2/WS_2 layered structure. (*Inset*) Photograph of synthetically synthesized bulk MoS_2 crystal. (*B*) Schematic representation of femtosecond pulsed laser ablation setup used for the fabrication of MoS_2 and WS_2 colloidal NPs. (*C*) Photo of colloidal solutions of laser-ablated MoS_2 NPs separated by the mean size of NPs by centrifugation at different rotation speeds: 200, 500, 1,000, 2,000, 4,000, and 8,000 rpm (from left to right). (*D*) Size distributions of laser-ablated MoS_2 NPs separated by the mean size of NPs by centrifugation at different rotation speed: 200, 500, 1,000, 2,000, 4,000, and 8,000 rpm. a.u., arbitrary units. (*E*) Real (ε_1) and imaginary (ε_2) parts of the dielectric function along the *ab*-plane and *c*-axis.

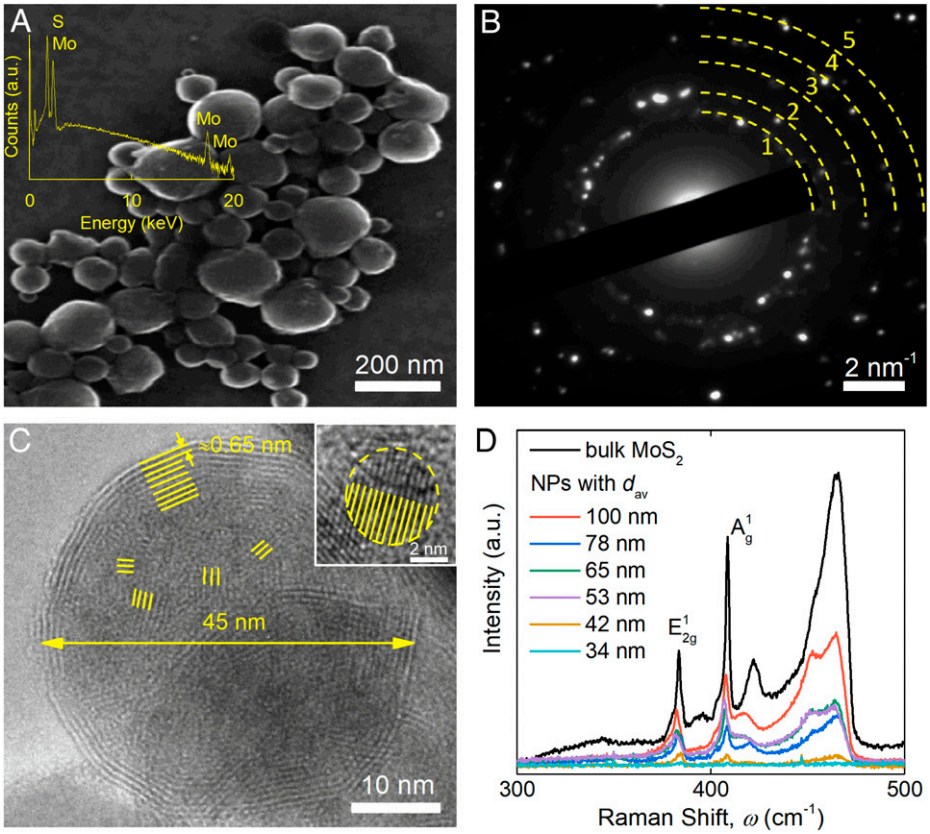

Fig. 2. Structure of MoS_2 NPs. (*A*) SEM image of laser-ablated MoS_2 NPs selected from a colloidal solution at 200 rpm. (*Inset*) The energy-dispersive X-ray spectrum of MoS_2 NPs on a Si substrate. (*B*) SAED pattern for laser-ablated MoS_2 NPs. (*C*) TEM image of 45-nm MoS_2 NP with a ring sequence typical for the hexagonal lattice. (*Inset*) A monocrystalline inner structure of 5-nm MoS_2 NP. Yellow lines highlight crystal planes. (*D*) Resonant Raman scattering spectra of laser-ablated MoS_2 NPs of different average sizes: 100, 78, 65, 53, 42, and 34 nm. The excitation wavelength is 633 nm.

generated as a result of minor oxidation during laser ablation in water. Meanwhile, selected area electron diffraction (SAED) images (Fig. 2*B* for MoS_2 and *SI Appendix*, Fig. S2*B* for WS_2) show a ring sequence typical for TMDCs with a hexagonal lattice. According to the Joint Committee on Powder Diffraction Standards (card no.: 75-1539), the rings labeled 1 to 5 in Fig. 2*B* correspond to the first five diffraction rings of the 2H-MoS_2 structure. The calculated lattice constants ($a = b = 0.32$ nm and $c = 1.39$ nm) from the rings correspond to lattice values for bulk MoS_2 from the literature (17). *SI Appendix*, Table S1 contains the final analysis findings of the SAED pattern. The internal structure of synthesized NPs was then examined using transmission electron microscopy (TEM). TEM data shown in Fig. 2*C* (for MoS_2) and *SI Appendix*, Fig. S2 *C* and *D* (for WS_2) evidence a polycrystalline core structure and a thick fullerene-like outer shell. A closer look reveals that the NP shell is not fully spherical and has a polygonal shape. This finding suggests that NP formation takes place along crystallographic axes, similar to the recently observed anisotropic crystallographic etching in TMDC during the lithography process (23).

At the same time, the smallest NPs (below 10 nm in diameter) demonstrate a well-developed layered structure and complete absence of the shell (Fig. 2*C*, *Inset*). Hence, one could expect them to inherit the original crystal's giant optical anisotropy (17). As a result, small TMDC NPs may pave the way for a new research field related to extremely anisotropic quantum dots. Finally, Raman spectroscopy was used to characterize the NPs (Fig. 2*D* and *SI Appendix*, Fig. S3). The characteristic Raman peaks ($E_{2g}^1 = 383$ cm^{-1} and $A_{1g} = 408$ cm^{-1}) perfectly matched the values reported for bulk MoS_2 (36), additionally demonstrating the excellent quality of produced NPs.

Optical Response of TMDC NPs. In light of the high crystallinity of synthesized NPs, one can expect them to exhibit bulk high refractive index and excitonic properties. The measured extinction curves (Fig. 3*A* and *SI Appendix*, Fig. S4) exhibit rich structure that agrees well with the predictions based on anisotropic constants from Fig. 1*D* and the extended Mie theory for radially anisotropic spheres (*Methods*) (37). As a result, optical properties of NPs mimic those of the original crystal, which opens up exciting possibilities for all-dielectric nanophotonics due to very high dielectric permittivity ($\varepsilon \sim 22$) of TMDCs in the visible range, much exceeding that of traditional high-refractive-index materials like Si ($\varepsilon \sim 14$) (38) and GaP ($\varepsilon \sim 10$) (39). Since the refractive index determines the capacity of NPs to control multipole moments and their ability to concentrate electromagnetic energy, one can expect the excitation of distinct Mie-multipole resonances from TMDCs nanostructures (38), particularly magnetic (MD) and electric dipole (ED) resonances (*SI Appendix*, Fig. S5). Fig. 3*A* clearly shows a blue shift of the MD resonance as the size of NPs decreases from 100 to 42 nm. Meanwhile, silicon NPs of the same size do not exhibit any features in the 1.5- to 2-eV (620 to 830 nm) spectral range, as follows from Fig. 3*B*. Moreover, MD and ED resonances appear near A- and B-excitons, as illustrated in Fig. 3*C*. Additionally, the high refractive index of MoS_2 leads to the excitation of Mie resonances that are substantially red-shifted compared to silicon NPs of the same size (Fig. 3*D*) and match the window of relative biological transparency (700 to 980 nm), which promises attractive theranostics (therapy + diagnostics) applications.

Photothermal Applications of TMDC NPs. Photothermal therapy of cancer (40) presents one of the most appealing implementations

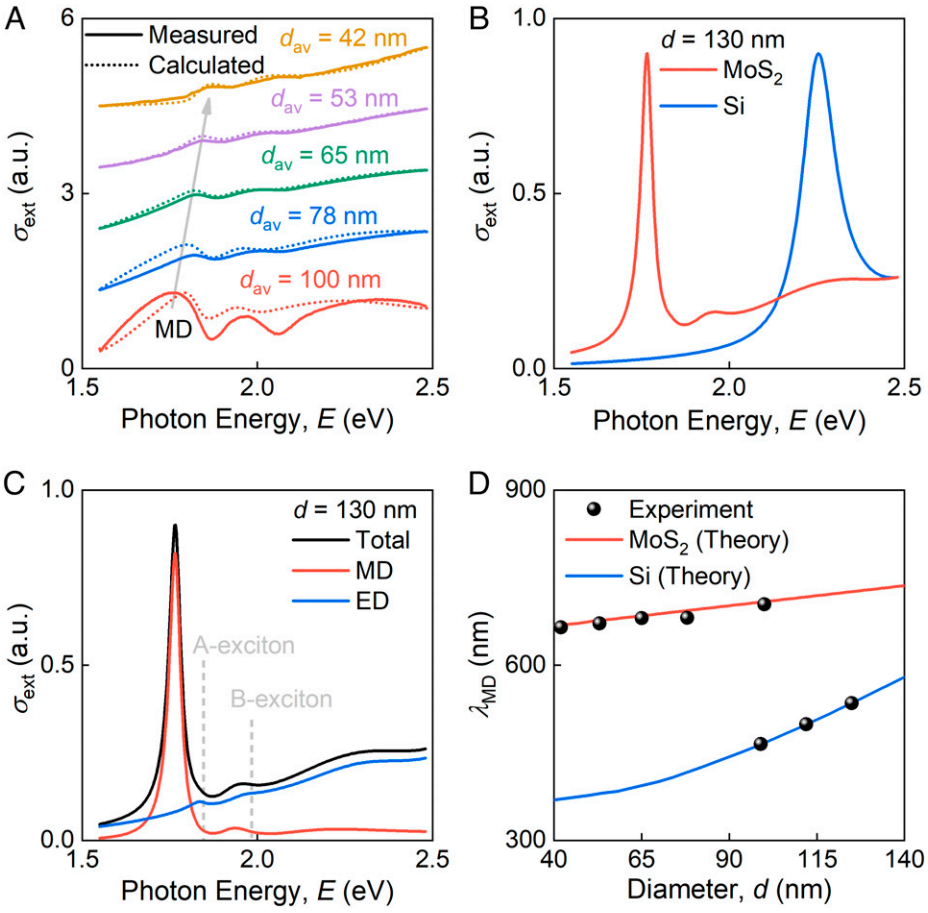

Fig. 3. Optical properties of MoS_2 NPs. (*A*) Extinction cross-section of colloidal MoS_2 NPs of different sizes indicated in the graph. Solid and dashed lines show experimental and calculated data, correspondingly. (*B*) Calculated extinction cross-section of 130 nm MoS_2 and Si NPs. (*C*) Multipole decomposition of extinction spectrum of a 130-nm MoS_2 NP. (*D*) Dependence of magnetic dipole (MD) peak position on the size of MoS_2 and Si NPs. a.u., arbitrary units.

of nanomedicine. Modern therapeutic approaches suggest combining efficient absorbing of light by complex resonant nanostructures in the window of relative biological transparency (41, 42) with enhanced optical contrast of such nanosystems (43). Besides that, photothermal therapy also requires efficient nanosensitizers to have a relatively small size (less than 100 nm) for a better transport in vivo and an enhanced uptake by the cells. However, this therapeutic modality requires efficient nanosensitizers absorbing in the tissue transparency window and having a relatively small size (less than 100 nm) for a better transport in vivo and an enhanced uptake by the cells. To assess the potential of laser-synthesized TMDC NPs for these applications, we investigated power-dependent Raman spectra from 65-nm MoS_2 and WS_2 NPs (Fig. 4 *A* and *B* and *SI Appendix*, Fig. S5 *A* and *B*). To determine heating efficiency, we assumed linear temperature T dependence of characteristic Raman peaks (E^1_{2g} and A_{1g}) position $\omega(T)$:

$$\omega(T) = \omega_0 + \chi_1 T,$$

where ω_0 is the peak position of modes at room temperature and χ_1 is the first-order temperature coefficient determined in the recent work (44). Consequently, we were able to recalculate the thermal shift of Raman peaks into the increase of local temperature (Fig. 4 *C* and *D* and *SI Appendix*, Fig. S5 *C* and *D*). Surprisingly, the temperature reached almost 800 K even at a very low excitation power of 300 μW, which was obviously due to drastically enhanced NP absorption boosted by the excitonic transitions, in contrast to unpatterned TMDC crystals (*SI Appendix*, Fig. S6). Apart from the 532- and 633-nm excitation wavelength used in Raman, we also tested the photothermal response of MoS_2 NPs at 830 nm in the therapeutic window (700 to 980 nm) and compared it with silicon NPs. The concentrations of NPs were normalized to the value of extinction at 830 nm (Fig. 4*E*). Under the same excitation conditions, MoS_2 NPs provided almost two times greater photothermal response than silicon NPs (Fig. 4*F*) due to a higher refractive index resulting in superior electromagnetic field concentration (38). Indeed, at 830 nm absorption cross-section of MoS_2 NPs with d_{av} = 65 nm is two times greater than for Si NPs with d_{av} = 140 nm. This high photothermal response makes TMDC NPs perfect biocompatible agents for photothermal applications.

In summary, we adopted methods of femtosecond laser ablation for the synthesis of TMDC spherical NPs of a controllable size and low size dispersion. Surprisingly, obtained NPs preserved the original crystal's layered structure and therefore demonstrated a unique combination of pronounced excitonic response and high refractive index value, which renders possible a strong concentration of electromagnetic field in NPs and the hybridization between the Mie and excitonic resonances. Such unique properties make TMDC NPs very promising candidates for a variety of all-dielectric nanophotonic applications where enhanced light–matter interaction via electromagnetic resonances plays a key role, including nanolasing (45), biosensing (46), photothermal cancer therapy (47), and nonlinear optics (48). Furthermore, in contrast to conventional lithographic

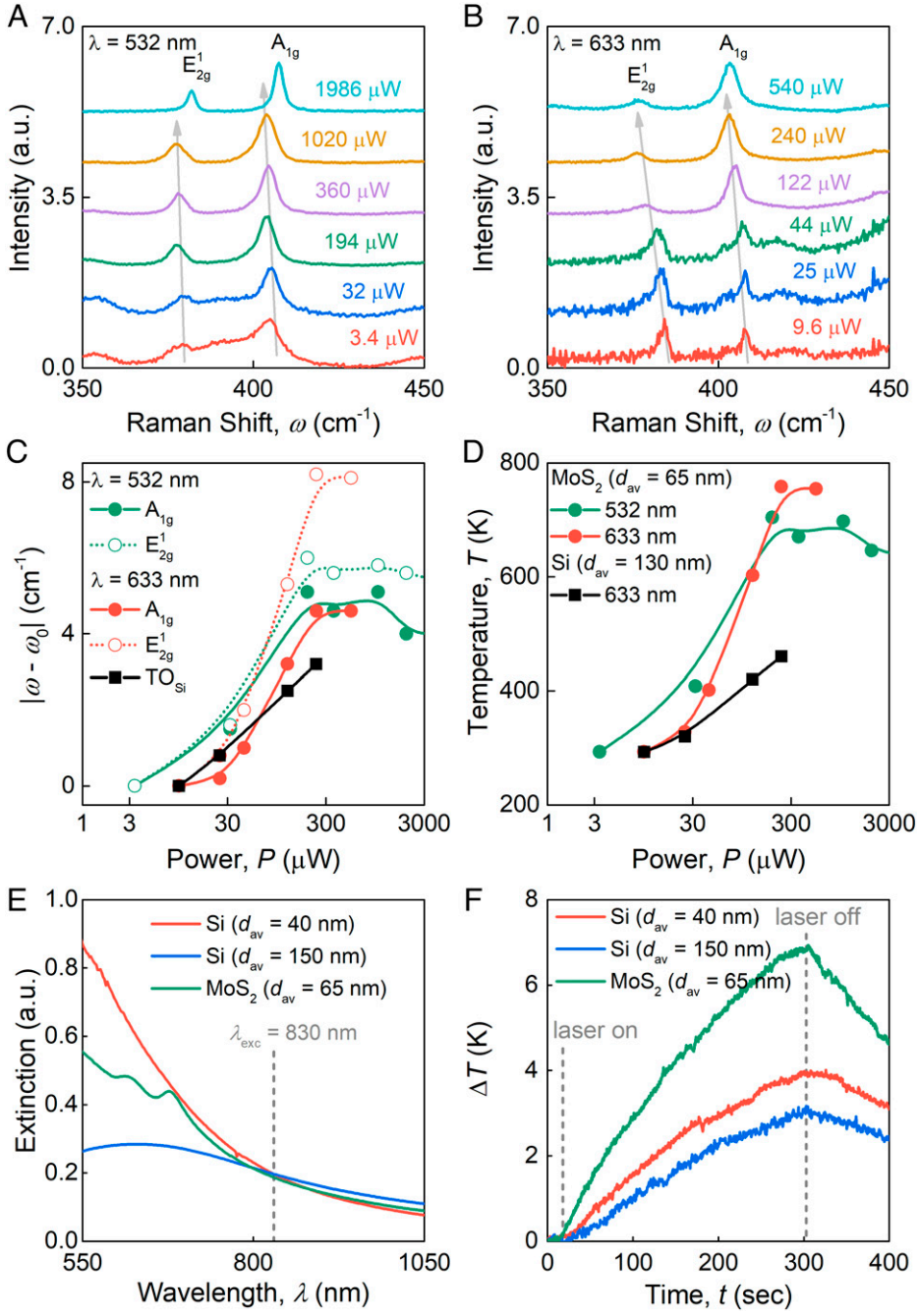

Fig. 4. Raman and photothermal responses of MoS_2 NPs. Raman spectra of 65 nm MoS_2 NPs on a glass substrate recorded under different laser excitation powers for two pumping wavelengths of 532 nm (*A*) and 633 nm (*B*). (*C*) Temperature shift of the frequencies corresponding to E^1_{2g} and A_{1g} Raman scattering modes of 65 nm MoS_2 NPs on a glass substrate for pumping wavelengths of 532 nm and 633 nm. For comparison, a shift of Si TO phonon mode for Mie-resonant 130 nm Si NPs under resonant 633 nm excitation is given. (*D*) Dependence of MoS_2 and Si NPs local temperature on the power *P* of excitation radiation for pumping wavelengths of 532 nm and 633 nm. (*E*) Extinction spectra of laser-ablated MoS_2 and Si NPs with different sizes used for photothermal measurements. Concentration of NPs was normalized at the excitation wavelength λ_{exc} = 830 nm. (*F*) Temperature growth of colloidal MoS_2 and Si solutions versus time during constant photothermal excitation with a power of *P* = 1 W at λ_{exc} = 830 nm. a.u., arbitrary units.

techniques for the fabrication of dielectric resonators, the proposed laser-ablative synthesis is substrate-free, high-throughput, and makes possible the fabrication of nanomaterials in mobile (colloidal) state, which promises the extension of TMDC-based materials to medical applications, including cancer therapy (47) and biomedical imaging (49). Finally, we believe our synthesis approach is universal for all layered materials such as MXenes (50), TMDCs (51), graphite (52), and hyperbolic materials (53). The fabrication of mobile nanostructures of these materials promises the development of postsilicon nanotechnology and a variety of novel attractive applications.

Methods

Sample Preparation. For the fabrication of TMDC NPs, we used a diode pump Teta 10 system (Avesta) with 100-μJ pulse energy at 1,030 nm and a repetition rate of 10 kHz. The laser beam was focused onto the surface of highly oriented synthetic 2H-phase MoS_2 and WS_2 crystals (2D Semiconductors Inc.) placed on the glass vessel bottom filled with deionized water. The process was carried out for 0.5 h at room temperature with a final NP concentration of about 0.1 mg/mL.

For the production of Si NPs with variable size we adopted the technique of femtosecond laser fragmentation from water-dispersed microcolloids reported previously (31). Briefly, 5 mL of aqueous solution of commercial Si micropowder (Goodfellow) with the concentration of 0.8 mg/mL was transferred into a glass

cuvette and subjected to laser irradiation by the laser beam from diode pump Teta 10 system (Avesta) with 270-fs pulse duration, 100-μJ pulse energy at 1,030 nm, and a repetition rate of 10 kHz. The laser beam was focused by a 75-mm lens onto the center of the cuvette, while the solution was stirred by a magnet to homogenize the ablation process. The duration of the fragmentation step was 2 h. Then, the colloidal solution of produced Si NPs was subjected to the centrifugation at increasing rotation speeds of 200 to 8,000 rpm to achieve monodisperse size distributions.

Structural Characterization. The atomic composition of the synthesized NPs was characterized by a scanning TEM system (MAIA 3; Tescan) operating at 0.1 to 30 kV coupled with an EDS detector (X-act; Oxford Instruments). Samples for SEM imaging were prepared by dropping 2 μL of the NP solution onto a cleaned silicon substrate with subsequent drying at ambient conditions. Morphological and structural properties of synthesized NPs were characterized by the high-resolution TEM system (JEM 2010; JEOL) operating at 200 kV with a Gatan Multiscan charge-coupled device in imaging and diffraction modes. Samples were prepared by dropping 2 μL of NPs solution onto a carbon-coated TEM copper grid and subsequent drying at ambient conditions. Analysis of SAED pattern was performed using ProcessDiffraction v.8.7.1 software.

Optical Characterization. Spectroscopic ellipsometry measurements were performed on an imaging Accurion nanofilm_ep4 ellipsometer over a wide wavelength range of 360 to 1,000 nm in steps of 1 nm at multiple incidence angles (50°, 55°, and 60°). The optical extinction spectra of colloidal NPs were measured using an ultraviolet-visible spectrophotometer (Cary 5000; Agilent Technologies) in a 500- to 800-nm (1.55 to 2.48 eV) spectral interval with the spectral resolution of 1 nm using 2-mm optical path length cuvettes. Raman scattering spectra were collected from NPs deposited on a glass substrate in backscattering geometry using a confocal scanning Raman microscope Horiba LabRAM HR Evolution. All measurements were carried out using linearly polarized excitation at wavelengths 633 nm and 532 nm, 1,800 lines per millimeter diffraction grating, whereas we used unpolarized detection to have a significant signal-to-noise ratio. Exciting radiation was focused on the sample surface with the ×100 objective (numerical aperture = 0.90) into the spot size of ∼0.5 μm.

Numerical Simulation. We used the extended Mie theory for spherical particles with radial anisotropy for numerical simulations (37). To achieve high accuracy, multipole expansion was carried out up to hexadecapole terms. Extinction spectra for NP solutions produced by centrifugation were calculated for spheres with diameters ranging from 6 nm to 500 nm with a step of 2 nm then averaged with weights corresponding to the fitted size distribution functions (Fig. 1*E*).

Multipolar Mode Decomposition. The multipole mode decomposition of the radiation is performed by applying the approach described previously (54). The fundamental multipole moments are evaluated by integrating the total electric field induced by a normally incident plane wave numerically inside the NP.

Data, Materials, and Software Availability. All study data are included in the article and/or *SI Appendix*.

ACKNOWLEDGMENTS. We gratefully acknowledge the financial support from the Ministry of Science and Higher Education of the Russian Federation (agreement 075-15-2021-606). Characterization of fabricated solutions of TMDC nanoparticles (G.I.T.) was supported by the Russian Science Foundation (grant 21-79-00206). Calculation of the extinction spectra (A.A.V.) was supported by the Russian Science Foundation (grant 22-79-10312). Fabrication of TMDC nanoparticles was supported by the Russian Science Foundation (grant 19-72-30012). K.S.N. acknowledges support from the Ministry of Education (Singapore) through the Research Centre of Excellence program (award EDUN C-33-18-279-V12, Institute for Functional Intelligent Materials) and the Royal Society (grant RSRP\R\190000).

Author affiliations: [a]Center for Photonics and 2D Materials, Moscow Institute of Physics and Technology, Dolgoprudny 141700, Russia; [b]Emerging Technologies Research Center, XPANCEO, Dubai Investment Park First, Dubai, United Arab Emirates; [c]Institute of Engineering Physics for Biomedicine (PhysBio), Bio-Nanophotonics Laboratory, National Research Nuclear University MEPhI, Moscow 115409, Russia; [d]Institute of Quantum Optics, Liebniz University Hannover, Hannover 30167, Germany; [e]CNRS, LP3, Aix-Marseille Université, Marseille 13288, France; [f]National Graphene Institute, University of Manchester, Manchester M13 9PL, United Kingdom; [g]Institute for Functional Intelligent Materials, National University of Singapore, Singapore 117574; and [h]Chongqing 2D Materials Institute, Chongqing 400714, China

Author contributions: A.S.T., A.A.V., A.V.S., S.M.N., A.V.K., A.V.A., and V.S.V. designed research; G.I.T., G.A.E., A.A.P., G.V.T., and D.A.P. performed research; S.M.K., A.B.E., and K.S.N. analyzed data; and K.S.N. and V.S.V. wrote the paper.

1. T. Mueller, E. Malic, Exciton physics and device application of two-dimensional transition metal dichalcogenide semiconductors. npj 2D Mater. *Appl.* **2**, 1–12 (2018).
2. Q. H. Wang, K. Kalantar-Zadeh, A. Kis, J. N. Coleman, M. S. Strano, Electronics and optoelectronics of two-dimensional transition metal dichalcogenides. *Nat. Nanotechnol.* **7**, 699–712 (2012).
3. G. Migliato Marega *et al.*, Logic-in-memory based on an atomically thin semiconductor. *Nature* **587**, 72–77 (2020).
4. A. Singh *et al.*, Refractive uses of layered and two-dimensional materials for integrated photonics. *ACS Photonics* **7**, 3270–3285 (2020).
5. Z. Sun, A. Martinez, F. Wang, Optical modulators with 2D layered materials. *Nat. Photonics* **10**, 227–238 (2016).
6. M. Cao *et al.*, Molybdenum derived from nanomaterials incorporates into molybdenum enzymes and affects their activities in vivo. *Nat. Nanotechnol.* **16**, 708–716 (2021).
7. Q. Han *et al.*, Molybdenum disulfide nanoparticles as multifunctional inhibitors against Alzheimer's disease. *ACS Appl. Mater. Interfaces* **9**, 21116–21123 (2017).
8. K. F. Mak, J. Shan, Photonics and optoelectronics of 2D semiconductor transition metal dichalcogenides. *Nat. Photonics* **10**, 216–226 (2016).
9. O. Lopez-Sanchez, D. Lembke, M. Kayci, A. Radenovic, A. Kis, Ultrasensitive photodetectors based on monolayer MoS_2. *Nat. Nanotechnol.* **8**, 497–501 (2013).
10. A. B. Laursen, S. Kegnaes, S. Dahl, I. Chorkendorff, Molybdenum sulfides–Efficient and viable materials for electro- and photoelectrocatalytic hydrogen evolution. *Energy Environ. Sci.* **5**, 5577 (2012).
11. Q. Li, N. Zhang, Y. Yang, G. Wang, D. H. L. Ng, High efficiency photocatalysis for pollutant degradation with MoS_2/C_3N_4 heterostructures. *Langmuir* **30**, 8965–8972 (2014).
12. G. Ermolaev *et al.*, Topological phase singularities in atomically thin high-refractive-index materials. *Nat. Commun.* **13**, 2049 (2022).
13. H. Hu *et al.*, Recent advances in two-dimensional transition metal dichalcogenides for biological sensing. *Biosens. Bioelectron.* **142**, 111573 (2019).
14. H. Chen, T. Liu, Z. Su, L. Shang, G. Wei, 2D transition metal dichalcogenide nanosheets for photo/thermo-based tumor imaging and therapy. *Nanoscale Horiz.* **3**, 74–89 (2018).
15. L. Gong *et al.*, Two-dimensional transition metal dichalcogenide nanomaterials for combination cancer therapy. *J. Mater. Chem. B Mater. Biol. Med.* **5**, 1873–1895 (2017).
16. F. Hu *et al.*, Imaging exciton-polariton transport in $MoSe_2$ waveguides. *Nat. Photonics* **11**, 356–360 (2017).
17. G. A. Ermolaev *et al.*, Giant optical anisotropy in transition metal dichalcogenides for next-generation photonics. *Nat. Commun.* **12**, 854 (2021).
18. A. A. Popkova *et al.*, Nonlinear exciton-Mie coupling in transition metal dichalcogenide nanoresonators. *Laser Photonics Rev.* **16**, 2100604 (2022).
19. A. Autere *et al.*, Optical harmonic generation in monolayer group-VI transition metal dichalcogenides. *Phys. Rev. B* **98**, 115426 (2018).
20. G. A. Ermolaev, D. I. Yakubovsky, Y. V. Stebunov, A. V. Arsenin, V. S. Volkov, Spectral ellipsometry of monolayer transition metal dichalcogenides: Analysis of excitonic peaks in dispersion. *J. Vac. Sci. Technol. B* **38**, 014002 (2020).
21. G. A. Ermolaev *et al.*, Broadband optical properties of monolayer and bulk MoS_2. npj 2D Mater. *Appl.* **4**, 1–6 (2020).
22. R. Verre *et al.*, Transition metal dichalcogenide nanodisks as high-index dielectric Mie nanoresonators. *Nat. Nanotechnol.* **14**, 679–683 (2019).
23. B. Munkhbat *et al.*, Transition metal dichalcogenide metamaterials with atomic precision. *Nat. Commun.* **11**, 4604 (2020).
24. R. Mupparapu *et al.*, Facile resist-free nanopatterning of monolayers of MoS_2 by focused ion-beam milling. *Adv. Mater. Interfaces* **7**, 2000858 (2020).
25. A. Castellanos-Gomez *et al.*, Laser-thinning of MoS_2: On demand generation of a single-layer semiconductor. *Nano Lett.* **12**, 3187–3192 (2012).
26. H. Lin *et al.*, Diffraction-limited imaging with monolayer 2D material-based ultrathin flat lenses. *Light Sci. Appl.* **9**, 137 (2020).
27. A. Kabashin *et al.*, Nanofabrication with pulsed lasers. *Nanoscale Res. Lett.* **5**, 454–463 (2010).
28. D. Zhang, B. Gökce, S. Barcikowski, Laser synthesis and processing of colloids: Fundamentals and applications. *Chem. Rev.* **117**, 3990–4103 (2017).
29. A. V. Kabashin, M. Meunier, Synthesis of colloidal nanoparticles during femtosecond laser ablation of gold in water. *J. Appl. Phys.* **94**, 7941 (2003).
30. J.-P. Sylvestre *et al.*, Surface chemistry of gold nanoparticles produced by laser ablation in aqueous media. *J. Phys. Chem. B* **108**, 16864–16869 (2004).
31. P. Blandin *et al.*, Femtosecond laser fragmentation from water-dispersed microcolloids: Toward fast controllable growth of ultrapure Si-based nanomaterials for biological applications. *J. Mater. Chem. B Mater. Biol. Med.* **1**, 2489–2495 (2013).
32. A. A. Popov *et al.*, Laser- synthesized TiN nanoparticles as promising plasmonic alternative for biomedical applications. *Sci. Rep.* **9**, 1194 (2019).
33. J. C. Bulmahn *et al.*, Laser-ablative synthesis of stable aqueous solutions of elemental bismuth nanoparticles for multimodal theranostic applications. *Nanomaterials (Basel)* **10**, 1463 (2020).
34. M. Kögler *et al.*, Bare laser-synthesized Au-based nanoparticles as nondisturbing surface-enhanced Raman scattering probes for bacteria identification. *J. Biophotonics* **11**, e201700225 (2018).
35. H. Wu *et al.*, Biocompatible inorganic fullerene-like molybdenum disulfide nanoparticles produced by pulsed laser ablation in water. *ACS Nano* **5**, 1276–1281 (2011).
36. X. Zhang *et al.*, Phonon and Raman scattering of two-dimensional transition metal dichalcogenides from monolayer, multilayer to bulk material. *Chem. Soc. Rev.* **44**, 2757–2785 (2015).

37. C.-W. Qiu, L.-W. Li, T.-S. Yeo, S. Zouhdi, Scattering by rotationally symmetric anisotropic spheres: Potential formulation and parametric studies. *Phys. Rev. E Stat. Nonlin. Soft Matter Phys.* **75**, 026609 (2007).
38. A. B. Evlyukhin *et al.*, Demonstration of magnetic dipole resonances of dielectric nanospheres in the visible region. *Nano Lett.* **12**, 3749–3755 (2012).
39. D. Khmelevskaia *et al.*, Directly grown crystalline gallium phosphide on sapphire for nonlinear all-dielectric nanophotonics. *Appl. Phys. Lett.* **118**, 201101 (2021).
40. D. Jaque *et al.*, Nanoparticles for photothermal therapies. *Nanoscale* **6**, 9494–9530 (2014).
41. R. E. Noskov *et al.*, Golden vaterite as a mesoscopic metamaterial for biophotonic applications. *Adv. Mater.* **33**, e2008484 (2021).
42. L. R. Hirsch *et al.*, Nanoshell-mediated near-infrared thermal therapy of tumors under magnetic resonance guidance. *Proc. Natl. Acad. Sci. U.S.A.* **100**, 13549–13554 (2003).
43. H. Li, X. Wang, T. Y. Ohulchanskyy, G. Chen, Lanthanide-doped near-infrared nanoparticles for biophotonics. *Adv. Mater.* **33**, e2000678 (2021).
44. S. Sahoo, A. P. S. Gaur, M. Ahmadi, M. J.-F. Guinel, R. S. Katiyar, Temperature-dependent Raman studies and thermal conductivity of few-layer MoS_2. *J. Phys. Chem. C* **117**, 9042–9047 (2013).
45. E. Tiguntseva *et al.*, Room-temperature lasing from Mie-resonant nonplasmonic nanoparticles. *ACS Nano* **14**, 8149–8156 (2020).
46. O. Yavas, M. Svedendahl, P. Dobosz, V. Sanz, R. Quidant, On-a-chip biosensing based on all-dielectric nanoresonators. *Nano Lett.* **17**, 4421–4426 (2017).
47. G. P. Zograf, M. I. Petrov, S. V. Makarov, Y. S. Kivshar, All-dielectric thermonanophotonics. *Adv. Opt. Photonics* **13**, 643 (2021).
48. C. Schlickriede *et al.*, Nonlinear imaging with all-dielectric metasurfaces. *Nano Lett.* **20**, 4370–4376 (2020).
49. A. Y. Kharin *et al.*, Bi-modal nonlinear optical contrast from si nanoparticles for cancer theranostics. *Adv. Opt. Mater.* **7**, 1801728 (2019).
50. B. Anasori, M. R. Lukatskaya, Y. Gogotsi, 2D metal carbides and nitrides (MXenes) for energy storage. *Nat. Rev. Mater.* **2**, 16098 (2017).
51. S. Manzeli, D. Ovchinnikov, D. Pasquier, O. V. Yazyev, A. Kis, 2D transition metal dichalcogenides. *Nat. Rev. Mater.* **2**, 17033 (2017).
52. Y. Hernandez *et al.*, High-yield production of graphene by liquid-phase exfoliation of graphite. *Nat. Nanotechnol.* **3**, 563–568 (2008).
53. W. Ma *et al.*, In-plane anisotropic and ultra-low-loss polaritons in a natural van der Waals crystal. *Nature* **562**, 557–562 (2018).
54. A. B. Evlyukhin, C. Reinhardt, E. Evlyukhin, B. N. Chichkov, Multipole analysis of light scattering by arbitrary-shaped nanoparticles on a plane surface. *J. Opt. Soc. Am. B* **30**, 2589 (2013).